

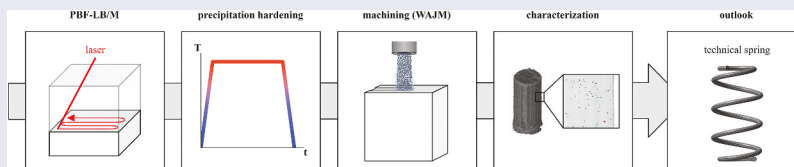
# The impact of additive manufacturing on the mechanical properties of a stainless precipitation hardening steel

Robert Brandt <sup>a</sup>, Frank Walther <sup>b</sup>, Jan T. Sehr <sup>c</sup>, Dirk Biermann<sup>d</sup>, Martin Lindner <sup>a</sup>, Felix Stern <sup>c</sup>, Tobias Grimm <sup>c</sup>, Sabrina Hase<sup>c</sup> and Meik Tilger<sup>d</sup>

<sup>a</sup>Materials Systems for Automotive Lightweight Design, University of Siegen, Siegen, Germany; <sup>b</sup>Chair of Materials Test Engineering, TU Dortmund University, Dortmund, Germany; <sup>c</sup>Hybrid Additive Manufacturing, Ruhr University Bochum, Bochum, Germany; <sup>d</sup>Institute of Machining Technology, TU Dortmund, Dortmund, Germany

## ABSTRACT

A stainless precipitation hardening steel has been qualified for powder bed fusion of metals using a laser beam. The mechanical and microstructural properties of additively manufactured samples have been thoroughly investigated and compared to samples of the very same material made by means of ingot casting. Additive manufacturing is feasible and can deliver superior mechanical properties. Additionally, the surface quality will be improved by means of wet abrasive jet machining, and its impact on the residual stresses has been shown.



## ARTICLE HISTORY

Received 26 August 2021  
Revised 16 November 2021  
Accepted 17 November 2021

## KEYWORDS

Precipitation hardening steel; PBF-LB/M; additive-subtractive-manufacturing; surface topography

## CLASSIFICATIONS

Methodology; apparatus; experimental design; Materials data analysis and utilization

## 1. Introduction

Technical springs are machine components that allow for absorbing of impacts and storing a high amount of mechanical energy. Hence, high strength steels are the preferred materials. While having a high-density  $\rho$ , high strength steels outperform most materials in terms of their specific yield strength  $YS/\rho$  at a moderate specific elastic modulus  $E/\rho$ . In mildly corrosive environments, an anti-corrosion coating sufficiently protects a technical spring made of steel. For an application in a more corrosive environment, however, the use of a stainless steel is mandatory. Therefore, the stainless precipitation hardening steel X1CrNiMoMnCu12-6.7-4.0-3.2-2.0 has been successfully qualified as a spring steel grade [1] for a conventional mass production technology comprising a YS of more than 1500 MPa.

As of today, there are only a few stainless precipitation hardening steels available for additive manufacturing (AM) technologies, let alone as spring steel grade. From the available literature, results for three precipitation hardening steels processed by means of AM technology are known. The impact of laser energy density on the microstructure formation and strength of the precipitation hardening steel 1.2709 is reported in [2]. Furthermore, a set of optimal parameters for

precipitation hardening tempering of such a steel 1.2709 is disclosed in Ref. [3]. However, this steel, having a Cr content of less than 0.25%, is not to be considered as a stainless steel. The stainless precipitation hardening steel 1.4542 (17-4 PH) was investigated in Ref. [4]. The reported steel is mostly austenitic, completely different from that of a wrought 17-4 PH steel, which is fully martensitic. The tensile properties are quite different from those of wrought 17-4 PH steel, i.e. having an upper yield point of 600 MPa, lower than expected from the microhardness (380 HV0.1). Therefore, 17-4 PH steel additively manufactured does not meet the above mentioned specification of YS. Investigations on the martensitic stainless precipitation hardening steel 1.4545 (15-5 PH) in Ref. [5] revealed a yield strength of 850 MPa at room-temperature, whereas the ASM handbook and a technical datasheet state a yield strength of about 1200 MPa at room temperature for wrought steel [6]. 15-5 PH steel additively manufactured does not meet the required specification of YS as well. Further, 15-5 PH tends to balling [7] and therefore to undesirable inhomogeneity. In summary, these steels are not yet suited, and there is still an urgent demand to identify an appropriate stainless steel as spring steel grade for AM. This work documents the first promising results

**CONTACT** Robert Brandt  [robert.brandt@uni-siegen.de](mailto:robert.brandt@uni-siegen.de)  University of Siegen, Am Eichenhang 50, Siegen 57076, Germany

This article has been corrected with minor changes. These changes do not impact the academic content of the article.

© 2022 The Author(s). Published by National Institute for Materials Science in partnership with Taylor & Francis Group

This is an Open Access article distributed under the terms of the Creative Commons Attribution License (<http://creativecommons.org/licenses/by/4.0/>), which permits unrestricted use, distribution, and reproduction in any medium, provided the original work is properly cited.

for such a qualification of the above mentioned stainless precipitation hardening steel X1CrNiMoMnCu-12-6.7-4.0-3.2-2.0. The examination of spring specific material properties is of primary importance. For this purpose, samples have been additively manufactured and examined. These results are compared to those of samples of the very same material made by means of ingot casting. Furthermore, the major process technology relevant properties of AM and surface treatment have been considered as well.

An AM process is described as the layer upon layer build-up of a three-dimensional workpiece and represents the third category next to subtractive and formative manufacturing [8]. One of the AM processes for the direct manufacturing of metal parts according to DIN EN ISO/ASTM 52900 is the powder bed fusion of metals using a laser beam system (PBF-LB/M), in which metal powder is molten and solidified layer upon layer by a focused laser beam. The quality of PBF-LB/M parts depends on the one hand on the metallic powder material and on the other hand on many process parameters. However, most important are in particular influencing variables, which relate to the laser-material interaction. Major research efforts in the scientific community have addressed the correlation between input parameters (particle size distribution, chemical composition, process parameters, strategies, etc.) and output parameters (mechanical properties, relative density, microstructure) [9,10]. To generate parts with sufficient mechanical properties, high surface quality and a high density, uniformly even and high-packed powder layers are required [11]. For this reason, the morphology of metal powder particles is important because it influences the flowability properties and powder bed densities [12,13]. Improved flowability of the powder material results in a shorter time to evenly distribute powder across the build platform. In many methods for determining the flowability, gravity pushes the powder through a funnel, according to DIN EN ISO 4490 and DIN EN ISO 13517, but is not able to determine the flowability in relation to the horizontal spread of the coater on the build platform [14–16]. An increase in absorptivity and thermal conductivity leads, on the one hand, to an increase in exposure speed and, on the other hand, to a reduction in laser power and thus to more economical exposure parameters. The influence of process parameters on the mechanical properties of PBF-LB/M parts such as part densities, porosities, and micro hardness, respectively, are typically analysed [17,18].

Due to the poor surface quality, post-machining processes are to be necessary for PBF-LB/M machined parts, especially when functionally relevant surface layer properties are required. Therefore, the fine abrasive machining process of wet abrasive jet machining (WAJM) is here considered as a special treatment option for PBF-LB/M machined parts. The WAJM process is allocated to machining processes with geometric undefined cutting edge and describes a force controlled process using an unbonded abrasive [19,20]. Typically, a fine abrasive of grain diameter less than  $d_K = 100 \mu\text{m}$  is sprayed using water as the carrier medium on the workpiece surface at high pressure [21–23]. The abrasive grain material itself, the abrasive grain geometry, and the average kinetic energy of the abrasive grain as well as the jet parameters are the major factors controlling the material removal and the resulting surface layer properties [20,24–26]. It is also known that the WAJM process implements beneficial compressional residual stresses at the surface layer due to the mechanical impacts of the abrasive grains [20,24,26].

## 2. Material samples and methods

The powder material was produced by argon gas atomization of a X1CrNiMoMnCu12-6.7-4.0-3.2-2.0 using a Laval nozzle, which created a metal powder with an average particle diameter size of  $d_{50} = 25 \mu\text{m}$ . The material composition of the additively manufactured samples (AMS) corresponds well to the block-cast samples (BCS) within the specification (s. Table 1).

Stability and variable flow rate were measured using the FT4 powder rheometer from Freeman Technology (UK). The reflectance of the samples was analysed at room temperature and ambient atmosphere with the Nicolet iS20 Fourier-transform infrared (FTIR) spectrometer from Thermo Fisher Scientific. The Pike DiffusIR was used as an accessory for the measurements.

The AMS were produced using the PBF-LB/M-system TruPrint 1000 of TRUMPF GmbH + Co. KG. The TruPrint 1000 is equipped with a Nd:YAG fibre laser (1070 nm wavelength) with a maximum laser power of 200 W and a focal diameter of  $30 \mu\text{m}$ . The components and the powder are protected against oxidation in the build chamber by a nitrogen gas atmosphere.

To evaluate the process ability of the powder material in the PBF-LB/M system, it is important to define a parameter window. The positioning and orientation of the samples as well as the configuration of the

**Table 1.** Chemical composition in wt. %, Fe balance.

Sample	Cr	Ni	Mo	Mn	Cu	Al	C
Specification	12 ± 0.5	6.7 ± 0.2	4.0 ± 0.2	3.2 ± 0.2	2.0 ± 0.1	0.45 ± 0.05	≤ 0.01
AMS	12	6.5	3.8	3.3	2.0	0.44	0.01
BCS	12	6.8	4.0	3.4	2.0	0.49	0.01

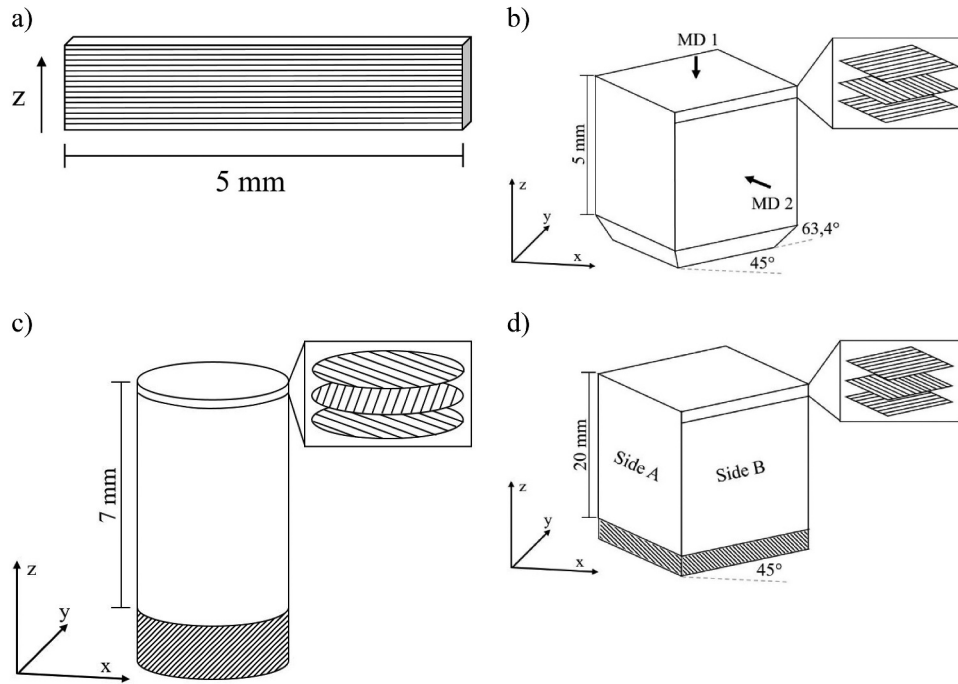


**Figure 1.** The geometries of (a) single track samples (AMS type a), (b) density samples (AMS type b) for quantitative phase analysis and hardness measurements with two measurement directions (MD), (c) test sample 1 (AMS type c) for compression test and  $\mu$ -CT investigations, and (d) test sample 2 (AMS type d) for micro-residual stress measurements and WAJM with two named sides.

exposure parameters were prepared by the processing software Materialise Magics from Materialise NV. The volume energy  $E_V$  is calculated by the laser power  $P_L$ , the scanning speed  $v_s$ , the hatch distance  $h_d$ , and the layer thickness  $D_S$ , as shown in Equation (1):

$$E_V = \frac{P_L}{v_s \times h_d \times D_S} \quad (1)$$

For a first assessment, stacked single tracks (AMS type a, s. Figure 1(a)) were generated with different laser powers and scanning speeds. The scanning speed varied between  $200 \text{ mm} \times \text{s}^{-1}$  and  $2000 \text{ mm} \times \text{s}^{-1}$ , and the nominal laser power varied between 60 and 170 W. The layer thickness was determined and kept constant at  $30 \text{ }\mu\text{m}$  based on the powder size distribution. By analysing the melt pool width of the stacked single tracks, a hatch distance for the following experiments was defined. For the determination of the relative density, cubes with an edge length of 5 mm were prepared (type b, s. Figure 1(b)). The cubes were directly connected to the build platform by an inverted pyramid with a height of 1 mm and an angle of  $63.4^\circ$ . A total of 25 samples with different volume energy densities were manufactured. Based on the evaluation of the stacked single tracks, the existing parameter window for the build process of the cubes was optimized. The scanning speed varied between  $400 \text{ mm} \times \text{s}^{-1}$  and  $1400 \text{ mm} \times \text{s}^{-1}$  with a step size of  $200 \text{ mm} \times \text{s}^{-1}$  and the nominal laser power varied between 80 W and 160 W with a step size of 20 W. The samples are manufactured with an overlap of 30% [27]. Therefore, the melt pool widths of the stacked single tracks were measured using the digital microscope

Keyence VHX 6000 from Keyence Corporation. Based on the mean values of these measurements, 70% of the measured melt pool widths were defined as unique hatch distances for every parameter set. For the mechanical characterization, microstructural analysis, and the surface treatments test specimens with  $d = 4 \text{ mm}$  and  $h = 7 \text{ mm}$  (AMS type c, Figure 1(c)) as well as cubes with  $a = 5 \text{ mm}$  (AMS type b, Figure 1(b)) and  $a = 20 \text{ mm}$  (AMS type d, Figure 1(d)) were built, respectively. The subsequent ageing of the test specimens happened by means of a circulating air furnace under argon atmosphere at a temperature  $T = 450^\circ\text{C}$  for a time  $t = 90 \text{ min}$ .

To analyze the microstructure and relative density of the samples, a digital microscope was used. To evaluate and compare the relative density, the entire cross-section  $A_{\text{extr}}$  of the filling section of a sample was recorded. The accumulated area  $A_{\text{pore}}$  of all pores can be determined by the aid of a particle/contamination analysis. The calculation of the relative density follows Equation (2):

$$\rho_{\text{rel}} = \frac{A_{\text{pore}}}{A_{\text{extr}}} \times 100\%. \quad (2)$$

A micro-residual stress analysis in the  $\alpha$  and  $\gamma$  phase, respectively, of a AMS happened by means of a PANalytical Empyrean XRD using  $\text{Cr-K}\alpha$  radiation (voltage  $U = 40 \text{ kV}$ , current  $I = 40 \text{ mA}$ , size of aperture  $5 \text{ mm} \times 5 \text{ mm}$ ). The  $z$  components  $\sigma_R$  of the micro-residual stress were measured at two sides of AMS type d, namely side A and side B, which are perpendicular to each other (s. Figure 1(d)), at the as built surfaces, before and after aging, respectively, as well as in post machined condition.

Due to severe rolling textures, the quantitative-phase analysis of a BCS requires a non-standard method as reported by Brokmeier [28]. For the sake of comparability, this method was applied for the AMS type d, as well. Hardness measurements generally happened into measuring direction MD 1 (s. Figure 1(b)), where each reported value represents the average of five indentations at the same sample of AMS type d. For the sake of completeness some hardness measurements into MD 2 are reported here as well.

X-ray micro-computed tomography ( $\mu$ -CT) scans were performed by means of a Nikon XT H 160 system for the non-destructive characterization of size, position, and shape of process-induced pores and defects. The reconstructed volumes were analysed with the software VGStudio Max 2.2. A detailed description can be found in Ref. [29], and the scanning parameters can be found in Table 2. With these parameters, a resolution or voxel size of  $9.5 \mu\text{m}$  could be realized resulting in a minimal detectable defect volume of  $6900 \mu\text{m}^3$  (8 voxel).

For mechanical characterization of the manufactured material, the specimens of AMS type c are used for compression tests at room temperature on a servo hydraulic testing system Schenck PSB100 with Instron 8800 controller (75 kN load cell) under displacement control ( $v_{c1} = 1.5 \times 10^{-3} \text{ mm} \times \text{s}^{-1}$  up to 0.3 mm compression;  $v_{c2} = 4.0 \times 10^{-2} \text{ mm} \times \text{s}^{-1}$  in the elastic-plastic region) according to DIN 50106. Since tensile testing was not feasible yet, compression tests successfully allow for a characterization of AMS, especially when only small amounts of powder material of a limited processing volume are available and different material conditions (e.g. process parameters, heat treatment) have to be evaluated [29,30].

The surface machining experiments are carried out on the wet abrasive jet machine type WA 110-P from Restec GmbH Nicolis Technology. The machine provides a maximum jet pressure of  $p_{st} = 10$  bar. The relative movement between the abrasive jet and the workpiece is realized by a six axis articulated robot IRB 44 from ABB Ltd, which moves the workpiece through the abrasive jet. For the investigation of the post-treatment surface topography by means of WAJM, the jet pressure  $p_{st}$  and the feed velocity  $v_f$  is varied each while keeping the other parameter constant, respectively. Aluminium oxide  $\text{Al}_2\text{O}_3$  (F220) with a nominal abrasive grain size of about  $d_K = 53 \dots 75 \mu\text{m}$  serves as abrasive medium using water as carrier medium.

The analysis focuses on the surface roughness and thus tactile and optical measurements were carried out on both the initial surfaces and the as machined

surfaces. For quantification of tactile roughness, measurements by means of the profilometer Mahrsurf XR20 were conducted. Additionally, nine measurements were made providing a statistical analysis by boxplots for each machined surface. Due to the workpiece geometry, the length for the tactile measurements was limited, so that the shorter length according to DIN EN ISO 4287 was used. Finally, all tactile measurements have been performed within a profile filter of  $\lambda_c = 0.8 \text{ mm}$  and a primary profile length of  $l_p = 4.8 \text{ mm}$ . The parameters calculated by the Mahr-internal software describes the industrially widely used mean roughness depth Rz, which was standardized in the former DIN EN ISO 4287 in 1984. Furthermore, confocal white-light measurements have been carried out using a Nanofocus  $\mu\text{surf}$  type C to qualitatively analyse the surface topography. For the optical measurements, a 50-magnification objective with a numerical aperture of 0.8 was used (type: Olympus 320-S).

### 3. Results

Table 3 shows the flowability characteristics of the powder sample. In accordance with other powders used in the PBF-LB/M process [31], the low basic flowability energy (BFE) of 771 mJ is characteristic for a powder with good flow properties. A small BFE value corresponds to a low resistance of the powder when being distributed or moved by the recoater or blade inside of the AM machine, which is positive for the PBF-LB/M process [13]. The specific energy (SE), measured during the upward movement of the blade, provides information about mechanical interlocking and cohesive forces between powder particles [31]. A value  $SE < 5$  indicates that the powder has low cohesion [32]. Here, the powder can move better and more freely, especially in the axial direction. The stability index (SI) indicates that the powder is a robust material of good flow stability and the flow rate index (FRI) close to the value 1 indicates that the reinforced powder is much less sensitive to flow rate, so that it can be considered a flow rate insensitive powder [31]. In summary, the flow properties are comparable to those of other powders used in PBF-LB/M and have a beneficial impact on the process.

The results of the reflectance measurement of the powder as indicator for absorption behaviour are presented in Figure 2. On the x-axis, the wavenumber is plotted, whereas the reflectance is plotted on the y-axis. The highlighted wavenumber of  $9345.8 \text{ cm}^{-1}$

**Table 2.** Parameters for  $\mu$ -CT analysis.

Acceleration voltage in kV	Beam current in $\mu\text{A}$	Exposure time in ms	Effective voxel size (resolution) in $\mu\text{m}$
160	76	250	9.5

**Table 3.** Flowability characteristics of the powder sample.

Basic flowability energy BFE in mJ	Stability index SI	Flow rate index FRI	Specific energy SE in mJ/g
$771.00 \pm 5.57$	$1.02 \pm 0.02$	$1.23 \pm 0.01$	$3.49 \pm 0.01$

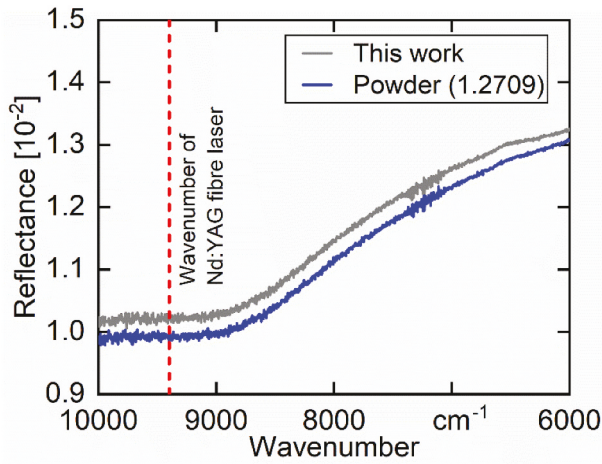


**Figure 2.** Reflectance measurement of two different powder feedstocks; reflectance was measured with respect to the wavenumber; wavenumber of  $9345.8\text{ cm}^{-1}$  corresponds to the laser wavelength of 1070 nm.

corresponds to a wavelength of 1070 nm. The measurement results in relative values of the reflectance, and are therefore plotted against a comparable powder material (1.2709, Trumpf). The graphs show a comparable trend and have similar values of  $1.020\% \pm 0.005\%$  and  $0.992\% \pm 0.002\%$  reflectance at a wavenumber of  $9345.8\text{ cm}^{-1}$ .

The hatch distances for the manufacturing of three-dimensional geometries were calculated from the melt pool widths of the stacked single tracks (Figure 3).

The parameters and relative density of the first studied samples are presented in Figure 4. The relative density ranges from 75.84% to 99.97%. The sample with a laser power of 160 W and a scanning speed of  $800\text{ mm} \times \text{s}^{-1}$  shows the highest relative density. To

Scanning Speed ( $\text{mm} \times \text{s}^{-1}$ )	Laser Power (W)				
	80	100	120	140	160
400	0.074	0.084	0.085		
600	0.067	0.077	0.074	0.084	0.085
800	0.063	0.064	0.073	0.083	0.078
1000	0.056	0.060	0.065	0.063	0.072
1200	0.055	0.056	0.063	0.061	0.065
1400				0.066	0.070

**Figure 3.** Different process parameters with unique hatch distances (mm) calculated from the melt pool widths.

verify this parameter window, the laser power and scanning speed were varied in 10% and 5% steps, respectively, around the best parameter set from the previous build process.

A different relative density with the same process parameters results from process deviations and is insignificant. According to VDI guideline 3405 sheet 2, parts manufactured by PBF-LB/M typically have a relative density of at least 99% [3]. As a result, there is not only one optimal parameter combination for parts with a sufficient relative density. As illustrated in Figure 4 the highest relative density of the second study, 99.94%, is achieved with a laser power of 174 W and a scanning speed of  $720\text{ mm} \times \text{s}^{-1}$ . Hence, these parameters are used to manufacture the test specimens for the investigation of the mechanical properties. Figure 5 presents the as-polished optical micrographs of the cube samples with the lowest and the highest achieved relative density using the above mentioned parameters.

Scanning Speed ( $\text{mm} \times \text{s}^{-1}$ )	Laser Power (W)									
	First study					Second study				
	80	100	120	140	160	144	152	160	168	174
400	75.84 ± 1.36	80.34 ± 2.14	84.45 ± 2.76			99.81 ± 0.13	99.85 ± 0.09	99.91 ± 0.02	99.89 ± 0.01	99.93 ± 0.02
600	79.95 ± 2.37	90.46 ± 2.20	94.37 ± 0.17	98.26 ± 0.48	99.63 ± 0.51	99.88 ± 0.04	99.89 ± 0.03	99.89 ± 0.02	99.93 ± 0.02	99.94 ± 0.02
800	91.45 ± 1.49	97.12 ± 1.05	99.76 ± 0.06	99.88 ± 0.05	99.97 ± 0.01	99.82 ± 0.07	99.89 ± 0.04	99.92 ± 0.03	99.88 ± 0.02	99.93 ± 0.04
1000	92.56 ± 1.05	96.21 ± 0.41	98.82 ± 0.52	99.90 ± 0.01	99.91 ± 0.01	99.85 ± 0.04	99.89 ± 0.07	99.89 ± 0.04	99.88 ± 0.05	99.89 ± 0.02
1200	89.92 ± 2.27	93.54 ± 0.67	96.72 ± 0.83	98.95 ± 0.12	99.65 ± 0.06	99.69 ± 0.10	99.78 ± 0.14	99.84 ± 0.03	99.89 ± 0.03	99.90 ± 0.02
1400				96.41 ± 1.14	97.93 ± 0.31					

**Figure 4.** Relative density (%) obtained from the cube samples with different process parameters. The second study is based on the best parameter set/density from the first study.

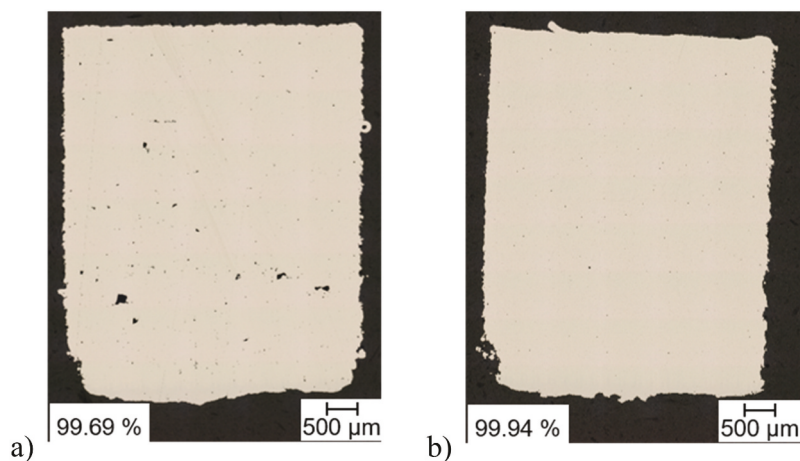


**Figure 5.** As-polished optical micrographs of (a) AMS (144 W, 960 mm × s<sup>-1</sup>) with low, and (b) AMS (174 W, 720 mm × s<sup>-1</sup>) with high relative density.

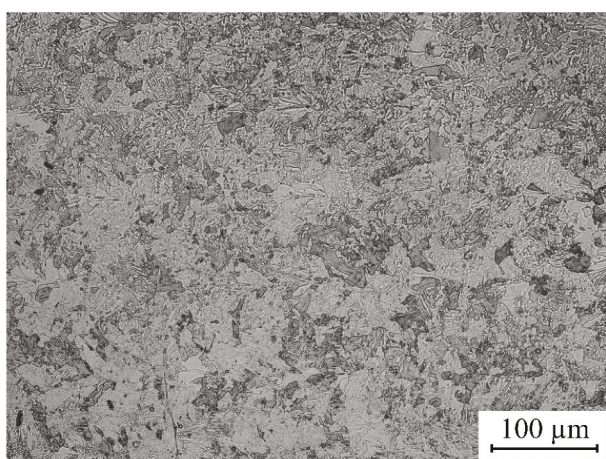


**Figure 6.** Cross-sectional micrograph of the test specimen via V2A etching.

The cross-sectional micrograph of AMS type d exhibits a much finer multiphase microstructure (s. [Figure 6](#)) than observed for a BCS [33]. A quantitative phase analysis reveals a volume fraction  $A = 13$  vol.-% of austenite (s. [Table 4](#)), which is by 6 vol.-% larger than that of the BCS. Due to aging, the austenite content significantly increases to become 23 vol.-%, exceeding that of the corresponding BCS by 9 vol.-%. The hardness of AMS type d  $H = 206 \pm 10$  HV10 is rather small compared to that of BCS (s. [Table 5](#)). Due to ageing, its hardness becomes  $H_{aged} = 350 \pm 12$  HV10, which is still much smaller than that of BCS.

As can be seen by the results of the  $\mu$ -CT scan ([Figure 7](#)), most of the detected pores in the specimen have a sphericity between 0.5 and 0.8. The overall detected density in the analysed region of interest was 99.99% which is in correspondence with the optical

**Table 4.** Austenite content  $A$  before and  $A_{aged}$  after ageing in vol.-%.

Sample	AMS type d (174 W, 720 mm × s <sup>-1</sup> )	BCS	AMS type b (144 W, 640 mm × s <sup>-1</sup> )
$A$	13	7	22
$A_{aged}$	23	14	28

**Table 5.** Vickers hardness  $H$  before and  $H_{aged}$  after ageing in HV10.

Sample	AMS type d (174 W, 720 mm × s <sup>-1</sup> )	BCS	AMS type b (144 W, 640 mm × s <sup>-1</sup> )
$H$	206 ± 10	281 ± 4	277 ± 35
$H_{aged}$	350 ± 12	405 ± 12	430 ± 112

imaging microscopy (OIM) investigations. The data obtained by the defect analysis was used to calculate the sphericity  $S$  and the equivalent diameter of a pore  $d_p$  using equation 6 and 7, respectively [34], where  $V$  is the volume of the defect and  $A$  the surface of the defect in  $\mu\text{m}^3$  and  $\mu\text{m}^2$ , respectively.

$$S = \frac{\pi^{\frac{1}{3}}(6V)^{\frac{2}{3}}}{A} \tag{6}$$

$$d_p = \sqrt[3]{\frac{6V}{\pi}} \tag{7}$$

While a value of 1 indicates a perfect sphere, the shape of a pore gets more and more aspherical and complex with lower values of  $S$ . Both the sphericity and the equivalent diameter are plotted and shown in [Figure 8](#). The results show that almost all pores have a sphericity between 0.5 and 0.8 and a maximum diameter of 76  $\mu\text{m}$ . The minimum diameter of pores found in the specimen was approximately 23  $\mu\text{m}$ .

The results of the compression tests are shown in [Figure 9](#) in terms of compressive stress – compressive strain curves. The step at approximately 5% compressive strain is related to the change in testing speed from  $v_{c1}$  to  $v_{c2}$ . Both shown curves are averaged curves with in total four specimens.

The compressive yield stress of the as built material is  $\sigma_{c,p0.2} = 437 \pm 13$  MPa and of the aged material  $452 \pm 29$  MPa, respectively (s. [Table 6](#)). Furthermore, the as built material has a pronounced hardening behaviour with a stress of  $1053 \pm 31$  MPa at  $\epsilon_c = 20\%$ , whereas the aged material requires only  $798 \pm 30$  MPa.

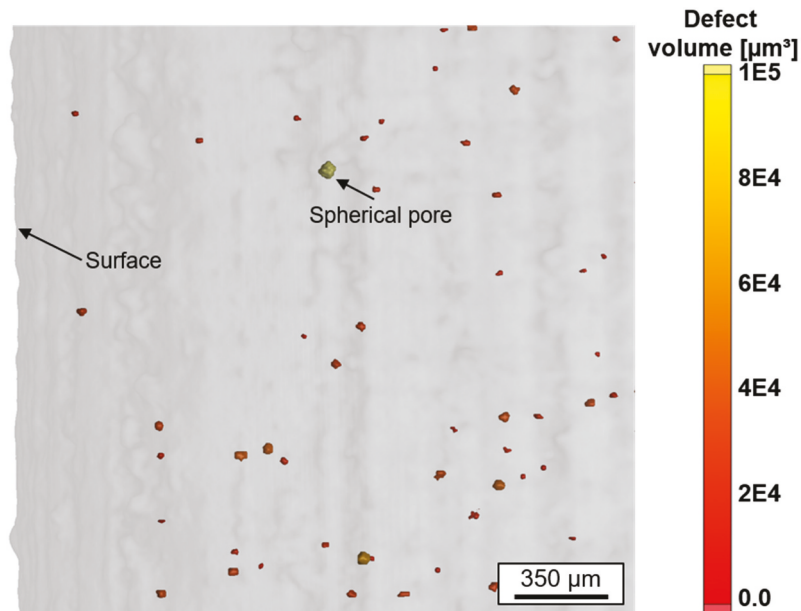


Figure 7. Magnified excerpt of the defect analysis by  $\mu$ -CT measurements.

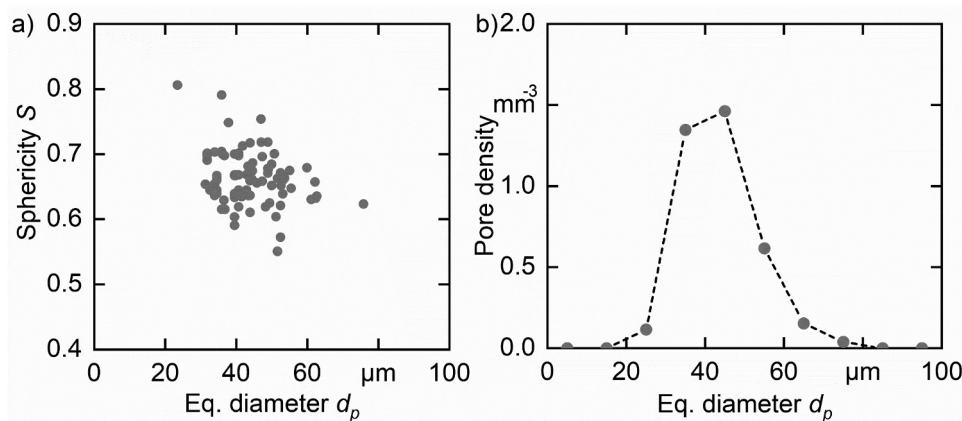


Figure 8. (a) Dependency of sphericity and equivalent pore diameter, (b) pore density of the AMS based on  $\mu$ -CT analysis.

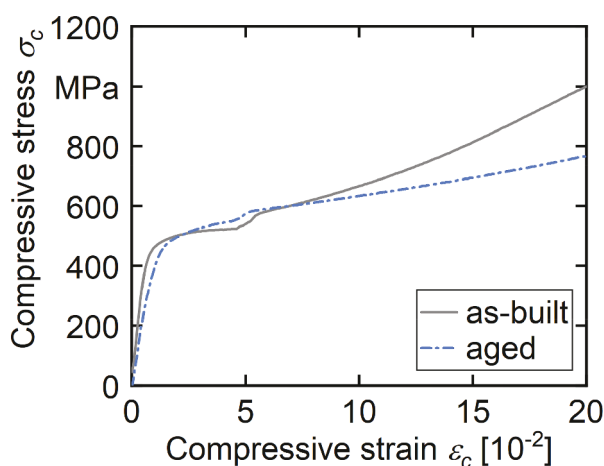


Figure 9. Results of compression tests. The step at around 5% compressive strain is due to the change in strain rate.

Table 6. Results of the compression tests of as built and aged specimens including standard deviation in MPa.

	$\sigma_{c,p0.2}$	$\sigma_{c,p2}$	$\sigma_{c,p20}$
As built	$437 \pm 13$	$511 \pm 8$	$1054 \pm 31$
Aged	$452 \pm 29$	$530 \pm 22$	$798 \pm 30$

Table 7. Micro-residual stresses  $\sigma_{R,\alpha}$  and  $\sigma_{R,\gamma}$  in z direction.

	$\sigma_{R,\alpha}$ at side A	$\sigma_{R,\alpha}$ at side B	$\sigma_{R,\gamma}$ at side A	$\sigma_{R,\gamma}$ at side B
As built	$-66 \pm 7$	$-110 \pm 30$	$-130 \pm 20$	$-195 \pm 24$
Aged	$-71 \pm 9$	$-120 \pm 24$	$-122 \pm 17$	$-177 \pm 20$
Post machined	$-845 \pm 23$	$-813 \pm 9$		

The z components of the micro-residual stress  $\sigma_R$  for both phases of AMS type d are compressive stresses in the as built state (s. Table 7), whereby the amount of  $\sigma_{R,\gamma}$  (austenite) is twice that of  $\sigma_{R,\alpha}$  (martensite) at both considered sides A and B, respectively. Due to ageing, the amount of compressive residual stress  $\sigma_{R,\alpha}$  slightly increases, while that of  $\sigma_{R,\gamma}$  slightly decreases. A qualitative phase analysis of the post-machined state reveals that no austenitic phase remains after the surface treatment. The absolute values of compressive residual stress  $\sigma_{R,\alpha}$  of the present entire martensitic phase become 845 MPa at side A and 813 MPa at side B, respectively.

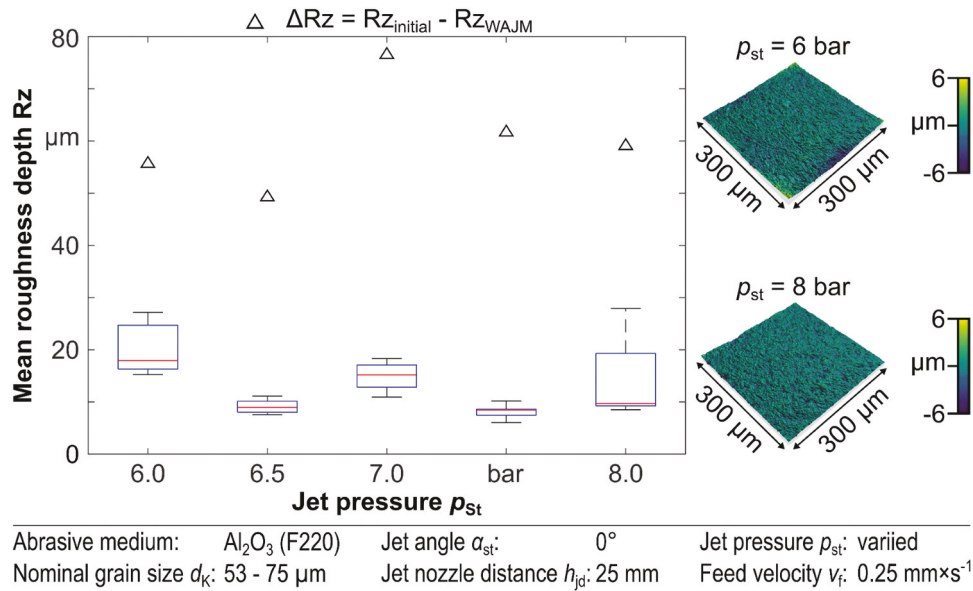


**Figure 10.** Boxplot diagram and exemplary 3D-topographies of wet abrasive jet machined surfaces by variation of the jet pressure  $p_{st}$ .

The mean roughness depth  $Rz_{initial}$  values of the as-built specimens are between 50  $\mu m$  and 110  $\mu m$ . The surface improvement according to WAJM is here reported by its change  $\Delta Rz$  of mean roughness depth with respect to the initial value  $Rz_{initial}$ . Figure 10 shows the boxplot diagram for the variation of jet pressure. The initial surface topography influences the results as well. However, based on the measurement results, no clear influence of the jet pressure can be identified, although, a small Rz-value of 8  $\mu m$  was achieved at  $p_{st} = 7.5$  bar. The three-dimensional topography shown in the figure on the right shows that for both jet pressures ( $p_{st} = 6$  bar and  $p_{st} = 8$  bar) an unidirectional and homogeneous topography has been generated by the process.

Figure 11 displays the results of different feed velocities  $v_f$  corresponding to different exposure times of the abrasive jet to the surface. Within an increasing feed velocity, the reduction  $\Delta Rz$  decreases. Accordingly, the lowest feed velocity  $v_f = 0.25 \text{ mm} \times \text{s}^{-1}$  generates the smoothest surface. Furthermore, the three-dimensional topographies show form deviations for the highest feed velocity  $v_f = 2.25 \text{ mm} \times \text{s}^{-1}$ . These effects can also be detected for all feed velocities  $v_f > 0.25 \text{ mm} \times \text{s}^{-1}$  and indicates insufficient surface treatment of the inhomogeneous and very rough initial topography, as the form deviations of the surface tend to increase with increasing feed rate.

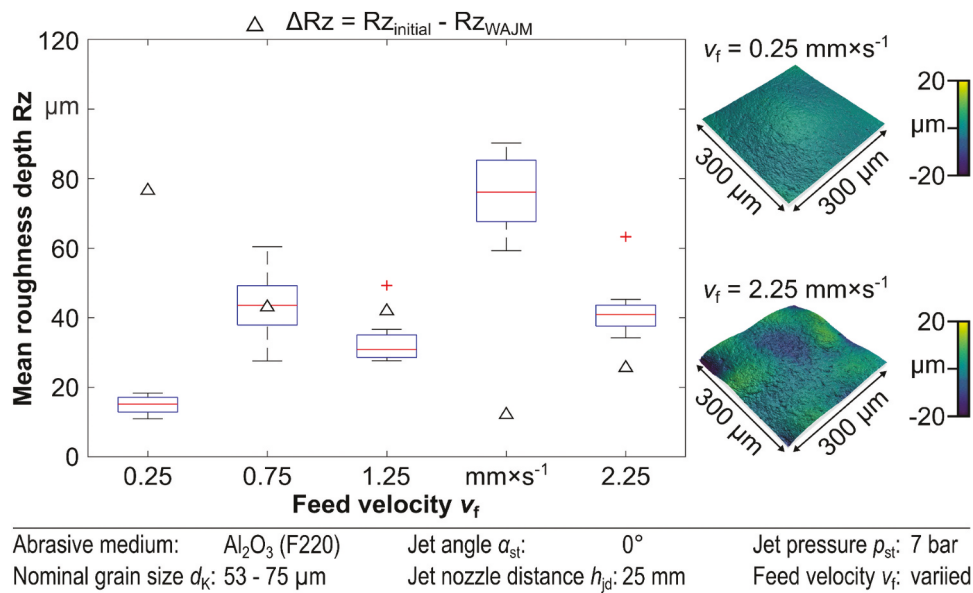


**Figure 11.** Boxplot diagram and exemplary 3D-topographies of wet abrasive jet machined surfaces by variation of the feed velocity  $v_f$ .

### 4. Discussion

Since only compression testing was feasible yet, the discussion mainly happens in terms of a Vickers hardness assessment, which correlates linearly with the tensile  $YS$  for the as aged BCS [33]. However, in terms of the here considered AMS type d, it shows an average hardness of  $H_{aged} = 350$  HV10 and a  $YS \sigma_{c,p0.2} = 452$  MPa under compression, which is lower than expected from the hardness. This is a feature that has also been reported by Facchini et al. [4]. The increase of hardness  $\Delta H = 144$  HV10 due to aging is close to that of BCS. In contrast to that, the nominal increase  $\Delta YS = 15$  MPa under compression is negligible. As shown in [33], this can be due to the huge amount  $A = 13\%$  of retained austenite and the additional formation of reversion austenite during aging leading to  $A_{aged} = 23\%$ . Compared with that of BCS, the  $H_{aged}$  value (s. Table 5) is rather small for AMS type d. Initially, this seems to be a detrimental result for the use as a spring steel, particularly with respect to the component's relative strength. Therefore, samples of AMS type b had been reconsidered with respect to their mechanical properties. The reduction of nominal laser power and scanning speed facilitates much higher  $H$  and  $H_{aged}$  values, respectively (s. Table 5, AMS type b (144 W,  $640 \text{ mm} \times \text{s}^{-1}$ )). However, the relative density is only marginally affected, i.e. by only 0.13%. As a matter of that result, a strategy for AM of precipitation hardening spring steels must not only pursue the goal of highest relative density, but also that of sufficient strength or hardness.

Interestingly enough,  $H_{aged}$  of AMS type b measured into MD 2 decreases with ascending position  $z$  (s. Figure 12), although the PBF-LB/M parameters have been kept constant throughout the production of the sample volume. It is assumed here that the local average temperature  $T = T(z)$  of the material during manufacturing is ascending as well. To achieve a material having constantly high  $H_{aged}$  values, either the PBF-LB/M parameters must be controlled accordingly or the whole manufacturing system must be designed for a more stable manufacturing process. A supervision of the local average temperature  $T(z)$  is beneficial for a low austenite content that does not contribute to precipitation hardening [35–37]. Prior investigations [33] show up that BCS of this material is susceptible to the formation of reversion austenite during the ageing process (s. Table 4). The very same effect has been observed for

AMS as well. Furthermore,  $A$  of AMS in the as built state is even bigger than that of BCS and there is some evidence that this is due to the formation of reversion austenite during the manufacturing process at a rather high local average temperature  $T(z)$  close to the top end of the AMS. The gradient in  $H_{aged} = H_{aged}(z)$  seems to be in line with our hypothesis. A control of  $T$  during PBF-LB/M might suppress the formation of reversion austenite so that lower values for  $A$  and higher values of  $H_{aged}$  become feasible. However, the investigated steel was developed for block-casting and the suitability for the PBF-LB/M process must be further improved by fine tuning the materials composition. For example, reducing austenite stabilizing elements such as Ni or Mn can reduce the amount of austenite, while also taking into account that Ni is a precipitation forming element [33,38].

The as built and aged conditions both show a very similar elastic behaviour, whereas the as built condition possesses a much higher strain-hardening behaviour. This can be explained by an incomplete transformation of austenite to martensite during the PBF-LB/M process. In the as built condition, the content  $A = 13\%$  is relatively high (Table 4). However, the  $A$  content in the aged condition of the samples was even higher, but showed significantly lower strain hardening. This indicates that the martensitic phase is responsible for the strain hardening behaviour. The BCS shows neither before nor after ageing a significant strain hardening comparably to AMS [1].

Further, the  $YS$  of the as quenched, as well as the aged BCS, are much higher than the ones of the AMS, namely 800 MPa and 1100 MPa, respectively [1]. However, the hardness values of the present AMS are inhomogeneous (s. Figure 12) so that the plastic deformation during the compression test occurs in the soft regions at high  $z$  values (s. Figure 1). Extrapolating the  $YS$  vs  $H$  plot of BCS indicates a  $YS$  of 500 MPa for  $H = 350$  HV10 [1] which fits to the revealed  $\sigma_{c,p0.2}$  value.

A possible explanation for the reduced hardening behaviour of the AMS in the aged condition could be the dissolution of the achieved fine microstructure, which is caused by the rapid cooling and solidification during the PBF-LB/M process. The finer microstructure including the known cellular subgrain structure possibly contributes to the strain hardening in the compression test through dynamic Hall-Petch effect [39]. This is

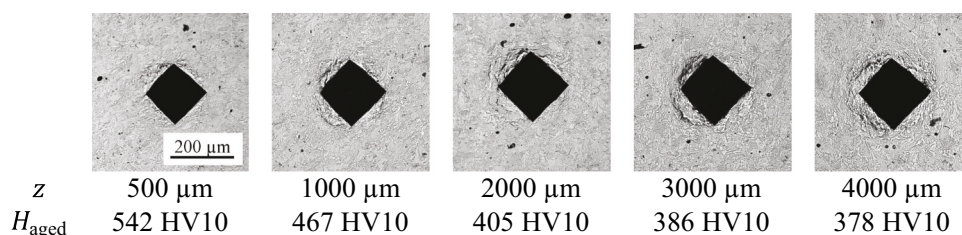


Figure 12. Vickers hardness  $H_{aged}$  indentations in MD 2 at the lateral surfaces of aged AMS type b at ascending positions of  $z$ .

linked to a high dislocation density in terms of a dislocation network embedded in individual grains and known to be present in the as built steel 1.4404 [40] and other materials such as CoCrFeNiMn high entropy alloy and pure copper, although the cause has not been conclusively clarified [41]. The shape of the dislocation network corresponds to the cellular subgrain structure and dislocations are concentrated at the wall of such cells. Under loading the dislocation movement is hindered and, thus, retarded by the cell walls [40] leading to an increased strengthening effect. Besides, the investigated steel consists of nickel martensitic matrix, which also have inherently a high dislocation density [42]. The visible differences in the elastic region are not further discussed, because due to the small specimen geometry and the general setup, the compressive strain could not be measured directly at the specimen and, thus, the Young's modulus does not reach the expected values. Further tests, especially tensile tests, have to be performed with sufficient specimen geometries.

The results of  $\mu$ -CT measurements (Figure 7) are in accordance with the micrographs and the metallographic porosity measurement. The detected density of 99.99% is higher than that assessed by means of micrographs. However, this is not unexpected, as  $\mu$ -CT is limited by its resolution and the quality of the scan, which is significantly influenced by the high density of the steel [43]. Nevertheless, it can be clearly seen that the detected porosity mostly consists of small pores mainly indicating gas or keyhole porosity. As no bigger and flat or aspherical defects can be found, it is concluded that the found process parameter window for the PBF-LB/M process is highly suitable for the investigated steel to produce nearly dense parts. Especially, the low scatter in the results of the compression tests support this assumption. This is supported by the further analysis of the pores shown in Figure 8(a). Almost all pores have a sphericity between 0.5 and 0.8, indicating that only a small amount of the pores are lack-of-fusion defects, which are mostly characterized as pores with  $S \leq 0.6$  [44]. Stern et al. found pores with a sphericity of approximately 0.3 in the PBF-LB/M stainless steel 1.4404, which were later identified as lack-of-fusion defects with remnant powder particles inside [34]. Mostly pores with a sphericity between 0.5 and 0.8 were also identified by Awd et al., who did  $\mu$ -CT scans of PBF-LB/M manufactured AlSi10Mg alloy [45]. The reported pore density is also comparable to the values found in this work (Figure 8(b)), although no pores with  $d_p > 100 \mu\text{m}$  were presented in the steel sample. However, a reason for this can be the much lower analysed volume of the cylindrical steel specimen reducing the probability of finding such a big defect.

The results for WAJM show that the initial surfaces influence the machined one, leading to different results due to deviations in the initial surface roughness. For this reason, the effects of the varied parameters jet pressure  $p_{st}$  and feed rate  $v_s$ , respectively, are

not as significant as expected. The chosen range for jet pressure of 6 bar to 8 bar may be too narrow to analyse the differences on a PBF-LB/M surface with initial Rz-values  $Rz > 50 \mu\text{m}$ . High feed rates seem to be further inappropriate, as the resulting topography shows shape deviations and thus seems to be machined inhomogeneously. With respect to the residual stresses, the initial surface deviations have been compensated and the compressive stresses have been increased. It could be assumed that different jet pressures in such a small range generate identical residual stress on the surfaces of the workpieces. However, it is possible that the depth curve of the residual stresses differs for different jet pressures.

## 5. Conclusions and outlook

In this work, precipitation hardening stainless steel has been successfully manufactured by a PBF-LB/M process with a density of up to 99.97%. However, the achieved as built hardness of the AMS are significantly lower than that of the as quenched BCS of the same material. Hence, the here described method to manufacture technical springs is not yet adequate. Extraordinary high hardness, which even surpasses that of BCS, is achieved in an AMS at a slightly reduced density of 99.81%. The required materials YS under compression of more than 1500 MPa has not been achieved. Hence, the impact of the PBF-LB/M parameters on the precipitation behaviour must be more thoroughly investigated in the future. The here considered scanning parameter ranges for laser power between 80 and 174 W and scanning speed between  $400 \text{ mm} \times \text{s}^{-1}$  and  $1400 \text{ mm} \times \text{s}^{-1}$ , respectively, may serve as baselines. Further measures for the validation of the here considered application seems to be mandatory or even highly recommended, namely:

- (1) An evolution of the here-applied steel grade may lead to a further reduction of austenite for improved mechanical properties, e.g. by a moderate reduction of Mn- or Ni-content.
- (2) The mechanical, corrosion, and corrosion fatigue properties of AMS must be validated at component level as well.
- (3) The microstructure of the material must be validated by means of modern methods of material science and technology to guarantee the quality of the entire manufacturing process of high-quality technical springs.
- (4) To meet the fatigue and corrosion fatigue specifications of technical springs, multi-stage machining must be validated for the required high-quality surface, such as that of a cold rolled blank with  $Rz = 4 \mu\text{m}$ , at component level.

## Acknowledgements

Part of this work was performed at the Micro- and Nanoanalytics Facility (MNAF) of the University of Siegen.

## Disclosure statement

No potential conflict of interest was reported by the author(s).

## ORCID

Robert Brandt  <http://orcid.org/0000-0001-7775-9662>  
 Frank Walther  <http://orcid.org/0000-0003-2287-2099>  
 Jan T. Sehrt  <http://orcid.org/0000-0001-5546-4580>  
 Martin Lindner  <http://orcid.org/0000-0003-3869-8945>  
 Felix Stern  <http://orcid.org/0000-0002-3974-8847>  
 Tobias Grimm  <http://orcid.org/0000-0002-1149-0506>

## References

- [1] Lindner M, Brandt R. Über den Einfluss von Mn auf die mechanischen Eigenschaften von nichtrostenden, martensitushärtenden Stählen. In: Christ H-J, editor. *Werkstoffprüfung 2019, Werkstoffe und Bauteile auf dem Prüfstand*. Sankt Augustin: INVENTUM GmbH; 2019. p. 181–186.
- [2] Kempen K, Yasa E, Thijs L, et al. Microstructure and mechanical properties of Selective Laser Melted 18Ni-300 steel. *Phys Procedia*. 2011;12255–12263. DOI:10.1016/j.phpro.2011.03.033
- [3] Verein Deutscher Ingenieure. VDI-Richtlinie 3405 Blatt 2: additive Fertigungsverfahren - Strahlschmelzen metallischer Bauteile - Qualifizierung, Qualitätssicherung und Nachbearbeitung; Berlin: Beuth Verlag GmbH 2013.
- [4] Facchini L, Vicente N, Lonardelli I, et al. Metastable austenite in 17-4 precipitation-hardening stainless steel produced by selective laser melting. *Adv Eng Mater*. 2010;12(3):184–188.
- [5] Roberts D, Zhang Y, Charit I, et al. A comparative study of microstructure and high-temperature mechanical properties of 15-5 PH stainless steel processed via additive manufacturing and traditional manufacturing. *Prog Addit Manuf*. 2018;3(3):183–190.
- [6] voestalpine BÖHLER Edelstahl GmbH & Co KG. Technical data sheet of 1.4545. [accessed 18 December 2021]. Available from: <https://www.bohler.de/de/lager-sortiment-vson/n701-bud/>
- [7] Islam M, Purtonen T, Piili H, et al. Temperature profile and imaging analysis of laser additive manufacturing of stainless steel. *Phys Procedia*. 2013;41835–41842. DOI:10.1016/j.phpro.2013.03.156
- [8] Gebhardt A. *Additive Manufacturing Und 3D-Drucken Für Prototyping-Tooling-Produktion: additive Fertigungsverfahren*. 5th ed. München: Hanser; 2016.
- [9] Zhang B, Dembinski L, and Coddet C. The study of the laser parameters and environment variables effect on mechanical properties of high compact parts elaborated by selective laser melting 316L powder. *Mater Sci Eng A*. 2013;584:21–31.
- [10] Sehrt JT. *Möglichkeiten und Grenzen bei der generativen Herstellung metallischer Bauteile durch das Strahlschmelzverfahren*. Duisburg: Universität Duisburg-Essen; 2010.
- [11] Kingsbury A. *Wohlers Report: 3d printing and additive manufacturing state of the industry*; 2016.
- [12] Zou RP, and Yu AB. Evaluation of the packing characteristics of mono-sized non spherical particles. *Powder Technol*. 1995;88:71–79.
- [13] Brika SE, Letenneur M, and Dion CA, et al. Influence of particle morphology and size distribution on the powder flowability and laser powder bed fusion manufacturability of Ti-6Al-4V alloy. *Addit Manuf*. 2020;31:1–16.
- [14] Clayton J, Millington-Smith D, Armstrong B. The application of powder rheology in additive manufacturing. *JOM*. 2015;67(3):544–548.
- [15] Lyckfeldt O, editor. *Powder rheology of steel powders for additive manufacturing*. Gothenburg: European Powder Metallurgy Association; 2013.
- [16] Mellin P, Lyckfeldt O, and Harlin P, editors. *Evaluating flowability of additive manufacturing powders, using the Gustavsson flow meter*. European Powder Metallurgy Association, Chantilly; 2016.
- [17] Cherry JA, Davies HM, Mehmood S, et al. Investigation into the effect of process parameters on microstructural and physical properties of 316L stainless steel parts by selective laser melting. *Int J Adv Manuf Technol*. 2015;76:869–879.
- [18] Wang D, Song C, and Yang Y, et al. Investigation of crystal growth mechanism during selective laser melting and mechanical property characterization of 316L stainless steel parts. *Mater Des*. 2016;100:291–299.
- [19] Deutsches Institut für Normung. *Fertigungsverfahren Spanen: Teil 0: allgemeines*; 2003 (DIN 8589-0).
- [20] Aßmuth R. *Schneidkantenpräparation durch Druckluft-Nassstrahlspanen mit Industrierobotern*. 1st ed. (Schriftenreihe des ISF; Vol. 99). Essen: Vulkan-Verlag GmbH; 2019.
- [21] Hashimoto F, Yamaguchi H, Krajnik P, et al. Abrasive fine-finishing technology. *CIRP Ann Manuf Technol*. 2016;65(2):597–620.
- [22] Köttnner D. *Herstellung von Schneidkantenverrundungen und deren Einfluss auf das Einsatzverhalten von Zerspanwerkzeugen*: Zugl.: Dortmund [Univ., Diss., 2006]. Dortmund: Vulkan-Verlag GmbH; 2006. (Schriftenreihe des ISF; vol. 36).
- [23] Terwey I. *Steigerung der Leistungsfähigkeit von Vollhartmetallwendelbohrern durch Strahlspanen*: Zugl.: Dortmund, Techn [Univ., Diss., 2011]. Essen: Vulkan-Verlag GmbH; 2011. (Schriftenreihe des ISF; vol. 63).
- [24] Denkena B, Biermann D. Cutting edge geometries. *CIRP Ann Manuf Technol*. 2014;63(2):631–653.
- [25] Biermann D, Aßmuth R, Schumann S, et al. Wet abrasive jet machining to prepare and design the cutting edge micro shape. *Procedia CIRP*. 2016;45195–45198. DOI:10.1016/j.procir.2016.02.071
- [26] Wolf M. *Abstimmung der Präparationsprozesse in der herstellungskette von PVD-beschichteten Vollhartmetall-Wendelbohrern*. 1st ed. (Schriftenreihe des ISF; Vol. 98). Essen: Vulkan-Verlag GmbH; 2019.
- [27] Di W, Yongqiang Y, Xubin S, et al. Study on energy input and its influences on single-track, multi-track, and multi-layer in SLM. *Int J Adv Manuf Technol*. 2012;58(9–12):1189–1199.
- [28] Brokmeier H-G. *Texturanalyse mittels winkeldispersiver neutronographischer Kernstreuung [Habilitationsschrift]*. Clausthal: Technische Universität Clausthal; 1995.
- [29] Doñate-Buendía C, Frömel F, Wilms MB, et al. Oxide dispersion-strengthened alloys generated by laser metal deposition of laser-generated nanoparticle-metal powder composites. *Mater Des*. 2018;154360–154369. DOI:10.1016/j.matdes.2018.05.044

- [30] Stern F, Grabienski F, Walther F, et al. Influence of powder nitriding on the mechanical behavior of laser-powder bed fusion processed tool steel X30CrMo7-2. *Mater Testing*. 2020;62(1):19–26.
- [31] Mussatto A, Groarke R, A-Hameed A, et al. Evaluation via powder metallurgy of nano-reinforced iron powders developed for selective laser melting applications. *Mater Des*. 2019;182108046. DOI:10.1016/j.matdes.2019.108046
- [32] Duckels C. *Specific energy*. Freeman Technology; Tewkesbury; 2008.
- [33] Brandt R, Lindner M. The application of a stainless martensitic precipitation hardening steel to an elastic spring. In: Weinrich, A. and Hermann, W., eds., *Verband der Deutschen Federnindustrie. 1st Compendium of Modern Spring Technologies 2021;Hagen; 2021*. p. 61 – 67. ISBN: 978-3-00-069928-3
- [34] Stern F, Tenkamp J, Walther F. Non-destructive characterization of process-induced defects and their effect on the fatigue behavior of austenitic steel 316L made by laser-powder bed fusion. *Prog Addit Manuf*. 2020;5(3):287–294.
- [35] Schnitzer R, Hochfellner R, Nöhner M, et al. Mikrostrukturelle Charakterisierung von PH 13-8 Mo Maraging-Stählen. *Pract Metallogr*. 2009;46(10):521–536.
- [36] Hossein Nedjad S, Movaghar Garabagh MR, Nili Ahmadabadi M, et al. Effect of further alloying on the microstructure and mechanical properties of an Fe–10Ni–5Mn maraging steel. *Mater Sci Eng A*. 2008;473(1–2):249–253.
- [37] Raabe D, Ponge D, Dmitrieva O, et al. Designing ultrahigh strength steels with good ductility by combining transformation induced plasticity and martensite aging. *Adv Eng Mater*. 2009;11(7):547–555.
- [38] Raabe D, Ponge D, Dmitrieva O, et al. Nanoprecipitate-hardened 1.5GPa steels with unexpected high ductility. *Scr Mater*. 2009;60(12):1141–1144.
- [39] Pham MS, Dovggy B, Hooper PA. Twinning induced plasticity in austenitic stainless steel 316L made by additive manufacturing. *Mater Sci Eng A*. 2017;704102–704111. DOI:10.1016/j.msea.2017.07.082
- [40] Liu L, Ding Q, Zhong Y, et al. Dislocation network in additive manufactured steel breaks strength–ductility trade-off. *Mater Today*. 2018;21(4):354–361.
- [41] Wang G, Ouyang H, Fan C, et al. The origin of high-density dislocations in additively manufactured metals. *Mater Res Lett*. 2020;8(8):283–290.
- [42] Jäggle EA, Choi -P-P, van Humbeeck J, et al. Precipitation and austenite reversion behavior of a maraging steel produced by selective laser melting. *J Mater Res*. 2014;29(17):2072–2079.
- [43] Aleshin NP, Grigor'ev MV, Shchipakov NA, et al. Applying nondestructive testing to quality control of additive manufactured parts. *Russ J Nondestruct Test*. 2016;52(10):600–609.
- [44] Snell R, Tammas-Williams S, Chechik L, et al. Methods for rapid pore classification in metal additive manufacturing. *JOM*. 2020;72(1):101–109.
- [45] Awd M, Stern F, Kampmann A, et al. Microstructural characterization of the anisotropy and cyclic deformation behavior of selective laser melted AlSi10Mg structures. *Metals*. 2018;8(10):825.